 CMC, vol.16, no.3, pp.273-293, 2010

Thermo-Elastic Localization Relationships for Multi-Phase Composites

Giacomo Landi[1] **and Surya R. Kalidindi**[2]

Abstract: In this paper, we present a computationally efficient multi-scale framework for predicting the local fields in the representative volume element of a multiphase material system subjected to thermo-mechanical loading conditions. This framework for localization relationships is a natural extension of our recent work on two-phase composites subjected to purely mechanical loading. In this novel approach, the localization relationships take on a simple structure expressed as a series sum, where each term in the series is a convolution product of local structure and the governing physics expressed in the form of influence coefficients. Another salient feature of this approach is its exploitation of discrete Fourier transforms (DFTs) in calibrating the localization relationships to numerical datasets produced by finite element models. In this paper, we extend and validate this new framework for localization relationships in two important ways: (i) application to thermo-mechanical loading conditions, and (ii) application to multi-phase composites.

Keywords: Thermoelasticity, composites, microstructure, DFT, FEM.

1 Introduction

Building on established statistical continuum theories (Beran 1968; Kroner 1986; Adams and Olson 1998; Garmestani, Lin and Adams 1998; Mason and Adams 1999; Lin and Garmestani 2000; Garmestani, Lin, Adams and Ahzi 2001; Saheli, Garmestani and Adams 2004), we have recently presented a novel approach (Kalidindi, Niezgoda, Landi, Vachhani and Fast 2009; Landi, Niezgoda and Kalidindi 2009) for predicting the elastic fields in three-dimensional (3-D) voxel-based microstructure datasets subjected to uniform periodic boundary conditions. At the core of this new framework are computationally efficient localization relationships that relate the imposed macroscale strain (or stress) tensor to its spatial distribution

[1] Department of Materials Science and Engineering, Drexel University, PA 19104
[2] correpsonding author. Department of Materials Science and Engineering, Department of Mechanical Engineering and Mechanics, Drexel University, PA 19104

at the microscale, while accounting for the topological details of the microstructure (Duvvuru, Wu and Kalidindi 2007; Binci, Fullwood and Kalidindi 2008; Kalidindi, Landi and Fullwood 2008; Fullwood, Kalidindi, Adams and Ahmadi 2009). These localization relationships are expressed as a polynomial series sum, where each successive term captures the contribution from a higher-order spatial correlation in the microstructure. In the approach originally described by Kroner (Kröner 1977; Kroner 1986), the values of the terms in the kernel function were established by selecting a reference medium and numerically evaluating a complex series of integrals. This approach leads to the principal value problem (the integrand exhibits a singularity in the domain of integration) and exhibits high sensitivity to the properties of the selected reference medium (Kalidindi, Binci, Fullwood and Adams 2006). In the improved framework presented recently by the authors (Kalidindi, Niezgoda et al. 2009; Landi, Niezgoda et al. 2009), the same series expressions were recast into much more computationally efficient representations using discrete Fourier transforms (DFTs) (Briggs and Henson 1995). The main advantage of using the DFT representations is that it allows easy calibration of the localization relationships to results from established numerical approaches such as the finite element methods. This novel approach circumvents all of the main obstacles associated with the principal value problem, precludes the need to select a reference medium, and produces much more accurate predictions.

In our recent work (Landi, Niezgoda et al. 2009), we have demonstrated the accuracy of the novel framework described above for a two-phase composite material system subjected to mechanical loading conditions. More specifically, we focused only on the first-order terms in the expansion and demonstrated that they provide highly accurate localization relationships for two-phase composite systems with up to moderate contrast in the properties of the constituent phases. It was also shown that the higher-order terms in the expansion are essential for composite systems with higher contrasts. These localization relationships are expected to serve as computationally efficient scale-bridging relationships in multi-scale materials modeling and design efforts. The overall approach can be seen as an efficient procedure for data-mining the results from computationally expensive numerical models, and establishing the underlying *knowledge systems* at a selected length scale in multi-scale modeling problems (Kalidindi, Niezgoda et al. 2009). The main advantage of building these knowledge systems is that they allow for compact representation of the knowledge extracted from the numerical simulations, and easy retrieval of the same knowledge as and when needed in a multi-scale modeling effort. They are also particularly well-suited for facilitating extremely fast explorations of the effects of changes in microstructure topology on the local fields of interest in the microstructure.

In this paper, we present the extension of the framework described above in two important directions. First, we undertake an extension of our recently developed localization relationships to include thermo-elastic response of composite material systems. After developing and presenting the needed enhancements to the framework, we demonstrate the accuracy of the framework for predicting local fields in example two-phase composite systems by comparing the predictions with the results from finite element models. Second, we present and validate a new scheme for applying the localization linkages to composite systems with more than two constituent phases.

2 Thermo-Elastic Localization Relationships

The macroscale (effective) thermo-elastic behavior of a composite can be expressed as

$$\overline{\boldsymbol{\sigma}} = \widetilde{\mathbf{C}} \left(\overline{\boldsymbol{\varepsilon}} - \widetilde{\boldsymbol{\alpha}} \theta \right), \tag{1}$$

where $\overline{\boldsymbol{\sigma}}$ is the macroscale symmetric second-rank Cauchy stress tensor, $\overline{\boldsymbol{\varepsilon}}$ is the macroscale symmetric total strain tensor (including both elastic and thermal components), $\widetilde{\mathbf{C}}$ is the symmetric fourth-rank effective stiffness tensor, $\widetilde{\boldsymbol{\alpha}}$ is the symmetric second-rank effective thermal expansion coefficients tensor, and θ is the imposed temperature change. Note that the effective stress and strain tensors are shown with a bar on the top to indicate that these are also the volume averaged quantities from the microscale (Hill 1952). On the other hand, the effective stiffness and thermal expansion tensors are generally not equal to the volume averaged values from the microscale. For purely thermal loading of the composite, we expect $\overline{\boldsymbol{\varepsilon}} = \widetilde{\boldsymbol{\alpha}} \theta$ and $\overline{\boldsymbol{\sigma}} = \mathbf{0}$. Therefore, it is convenient to decompose the overall macroscale strain on the composite into two components: (i) $\overline{\boldsymbol{\varepsilon}}^m = \left(\overline{\boldsymbol{\varepsilon}} - \widetilde{\boldsymbol{\alpha}} \theta \right)$ can be visualized as the effective mechanical component, and (ii) $\overline{\boldsymbol{\varepsilon}}^{th} = \widetilde{\boldsymbol{\alpha}} \theta$ as the effective thermal component. However, it is important to recognize that neither the local elastic strain nor the local stress tensor fields at the microscale are generally zero-valued tensor fields for the purely thermal loading condition.

For considerations at the microscale, we start with a discrete representation of the microstructure consistent with the datasets produced by modern materials characterization equipment. We assume that the representative volume element (RVE) of the composite's internal structure is binned into a uniform grid of spatial cells (or voxels) that are enumerated by a three-dimensional vector $\boldsymbol{s}$ whose components take only integer values. Let $\mathbf{S}$ and $|\mathbf{S}|$ represent the complete set of all spatial cells and the total number of spatial cells, respectively, in the given dataset. The microstructure datasets typically identify the local state in each cell. The set of all

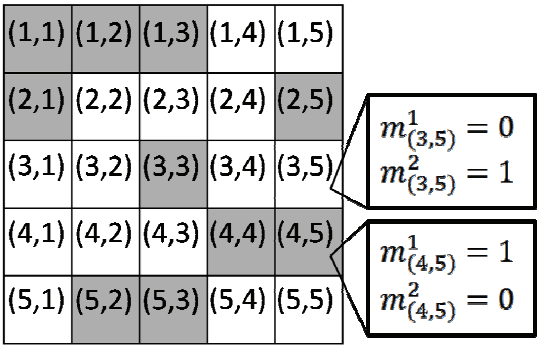

Figure 1: The microstructure variable, $m^h_{\mathbf{s}}$, identifies the volume fraction of material associated with the local state h in the spatial bin $\boldsymbol{s}$. In the simple two-dimensional microstructure shown here, the spatial cells are enumerated by a two-component vector as shown. The composite is comprised of two phases that are denoted as gray and white (H=2). h=1 identifies the gray colored phase, and h=2 the white colored phase in the figure above. The values of the microstructure variable in spatial cells (3,5) and (4,5) take the values shown on the right.

distinct local states that are possible in a given material system is referred to as the local state space. In this work, the local state space of interest is also assumed to be tessellated into individual bins and enumerated by h=1,2,...,H. For example, in a three-phase composite, H = 3. The variable $m^h_{\mathbf{s}}$ then defines the volume fraction of local state h in the spatial cell $\boldsymbol{s}$. Figure 1 further clarifies the definition of the microstructure variable. Based on this definition of the microstructure variable (Adams, Gao and Kalidindi 2005; Fullwood, Niezgoda and Kalidindi 2008; Niezgoda, Fullwood and Kalidindi 2008; Fullwood, Niezgoda, Adams and Kalidindi 2009), it is easy to establish the following properties:

$$\int_{h=1}^{H} m^h_{\mathbf{s}} = 1, \qquad m^h_{\mathbf{s}} \geq 0, \qquad \frac{1}{|\mathbf{S}|} \sum_{\mathbf{s} \in \mathbf{S}} m^h_{\mathbf{s}} = V^h \tag{2}$$

where V^h denotes the volume fraction of local state h in the microstructure dataset being studied.

Building on the pioneering work of Kroner (Kroner 1986), we have recently formulated and validated a new framework for expressing the localization relationship for the spatial distribution of the elastic strain at the microscale in the case of a composite subjected to purely mechanical loading condition (Kalidindi, Niezgoda et al. 2009; Landi, Niezgoda et al. 2009). For the thermo-mechanical loading conditions considered here, this localization relationship expressed as a series can be

exercised directly for the mechanical component as

$$\boldsymbol{\varepsilon}_{\mathbf{s}}^{m} = \left(\sum_{h=1}^{H} \sum_{\mathbf{t} \in \mathbf{S}} \boldsymbol{\alpha}_{\mathbf{t}}^{h} \, m_{\mathbf{s}+\mathbf{t}}^{h} + \sum_{h=1}^{H} \sum_{h'=1}^{H} \sum_{\mathbf{t} \in \mathbf{S}} \sum_{\mathbf{t}' \in \mathbf{S}} \boldsymbol{\alpha}_{\mathbf{t}\mathbf{t}'}^{hh'} \, m_{\mathbf{s}+\mathbf{t}}^{h} m_{\mathbf{s}+\mathbf{t}+\mathbf{t}'}^{h'} + \ldots \right) \overline{\boldsymbol{\varepsilon}}^{m} \tag{3}$$

where $\boldsymbol{\varepsilon}_{\mathbf{s}}^{m}$ denotes the local elastic strain tensor due to the overall imposed mechanical strain component, $\boldsymbol{\alpha}_{\mathbf{t}}^{h}$ and $\boldsymbol{\alpha}_{\mathbf{t}\mathbf{t}'}^{hh'}$ are fourth-rank tensors that are completely independent of $m_{\mathbf{s}}^{h}$, and are referred to as *influence coefficients* (Kalidindi, Niezgoda et al. 2009; Landi, Niezgoda et al. 2009). The $\boldsymbol{\alpha}_{\mathbf{t}}^{h}$ coefficients capture the first-order contribution to $\boldsymbol{\varepsilon}_{\mathbf{s}}^{m}$ from the presence of local state h in a spatial bin that is vector $\boldsymbol{t}$ away from the spatial bin of interest, $\boldsymbol{s}$. In a similar manner, $\boldsymbol{\alpha}_{\mathbf{t}\mathbf{t}'}^{hh'}$ coefficients capture the second-order contribution to $\boldsymbol{\varepsilon}_{\mathbf{s}}^{m}$ from simultaneous presence of local states h and h' in spatial cells $\boldsymbol{t}$ and $\mathbf{t}+\mathbf{t}'$ from the spatial bin of interest, $\boldsymbol{s}$, respectively.

As demonstrated in our recent work (Binci, Fullwood et al. 2008; Kalidindi, Landi et al. 2008; Fullwood, Kalidindi et al. 2009; Landi, Niezgoda et al. 2009), the most accurate values of the influence coefficients are established by calibrating Eq. (3) to numerical results obtained from finite element models. In order to accomplish this calibration, it is highly advantageous to recast Eq. (3) using discrete Fourier transform (DFT) representations as

$$\mathfrak{I}_{\mathbf{k}} \left(\boldsymbol{\varepsilon}_{\mathbf{s}}^{m} \right) = \left[\left(\sum_{h=1}^{H} \left(\boldsymbol{\beta}_{\mathbf{k}}^{h} \right)^{*} M_{\mathbf{k}}^{h} \right) + \left(\sum_{h=1}^{H} \sum_{h'=1}^{H} \left(\boldsymbol{\beta}_{\mathbf{k}}^{h} \right)^{*} \sum_{\mathbf{r} \in \mathbf{S}} \left(\boldsymbol{\beta}_{\mathbf{r}}^{'h'} \right)^{*} M_{\mathbf{r}}^{h'} M_{\mathbf{k}-\mathbf{r}}^{h} \right) + \ldots \right] \overline{\boldsymbol{\varepsilon}}^{m} \tag{4}$$

$$\boldsymbol{\beta}_{\mathbf{k}}^{h} = \mathfrak{I}_{\mathbf{k}} \left(\boldsymbol{\alpha}_{\mathbf{t}}^{h} \right), \quad M_{\mathbf{k}}^{h} = \mathfrak{I}_{\mathbf{k}} \left(m_{\mathbf{s}}^{h} \right) \tag{5}$$

where $\mathfrak{I}_{\mathbf{k}}()$ represents the DFT operation with respect to the spatial variables $\boldsymbol{s}$ or $\boldsymbol{t}$, and the star in the superscript denotes the complex conjugate. As a further clarification, $\mathfrak{I}_{\mathbf{k}}(\,)$ acts on all $\mathbf{s}$ or $\boldsymbol{t}$ in the RVE. Since the spatial bins are defined here in three-dimensions, the DFT operator defined in Eq. (5) acts on the 3-D arrays. Although the total number of influence coefficients in Eq. (3) and in Eq. (4) remains the same, Eq. (4) allows us to establish their values in smaller sets by standard linear regression analyses methods. For example, in the first-order term, indices $\boldsymbol{t}$ and h are completely coupled to each other in Eq. (3), while the summation on $\boldsymbol{k}$ vanishes in Eq. (4). This is extremely beneficial in performing regression analysis because it is much easier to establish H coefficients at a time and repeat the procedure $|\mathbf{S}|$ times, than it is to establish $|\mathbf{S}|H$ coefficients all at once. Noting that $|\mathbf{S}|$ is typically a very large number, it is easy to see the benefits of using the DFT representations.

We confine our interest here to only the first-order influence coefficients in the localization relationships. As noted in our prior work (Kalidindi, Niezgoda et al. 2009; Landi, Niezgoda et al. 2009), this is adequate for low and moderate contrast composites. The effort involved in establishing the higher-order terms is substantially larger, and is out of the scope of the present work (note the number of influence coefficients in the second-order terms is $(|\mathbf{S}|\ H)^2$).

The constraints implicit in the definition of the microstructure function (see Eq. (2)) translate to the following requirements in DFT space:

$$\sum_{h=1}^{2} M_{\mathbf{0}}^{h} = |\mathbf{S}|\,, \qquad \sum_{h=1}^{2} M_{\mathbf{k}\neq\mathbf{0}}^{h} = 0. \tag{6}$$

Introducing Eq. (6) into Eq. (4) removes the redundancies implicit in Eq. (4) and yields the following expression (considering only the first-order terms):

$$\mathfrak{I}_{\mathbf{k}\neq\mathbf{0}}\left(\boldsymbol{\varepsilon}_{\mathbf{s}}^{m}\right) = \left[\left(\widehat{\boldsymbol{\beta}}_{\mathbf{k}}^{1}\right)^{*} M_{\mathbf{k}}^{1}\right]\left(\overline{\boldsymbol{\varepsilon}}^{m}\right), \quad \mathfrak{I}_{\mathbf{0}}\left(\boldsymbol{\varepsilon}_{\mathbf{s}}^{m}\right) = |\mathbf{S}|\,\overline{\boldsymbol{\varepsilon}}^{m}, \quad \widehat{\boldsymbol{\beta}}_{\mathbf{k}}^{1} = \left(\boldsymbol{\beta}_{\mathbf{k}}^{1} - \boldsymbol{\beta}_{\mathbf{k}}^{2}\right). \tag{7}$$

The expression for $\mathfrak{I}_{\mathbf{0}}\left(\boldsymbol{\varepsilon}_{\mathbf{s}}^{m}\right)$ in Eq. (7) simply imposes the requirement that the volume average of $\boldsymbol{\varepsilon}_{\mathbf{s}}^{m}$ over the microscale should be equal to the $\overline{\boldsymbol{\varepsilon}}^{m}$ imposed at the macroscale.

For the macroscale imposed thermal component, $\overline{\boldsymbol{\varepsilon}}^{th} = \widetilde{\boldsymbol{\alpha}}\theta$, we develop here a localization relationship using the same approach as described above. However, since we do not know the macroscale thermal component of the strain a priori (since $\widetilde{\boldsymbol{\alpha}}$ is expected to be a strong function of the microstructure, it is not generally already known) and we do know that the volume averaged stress tensor arising from this component of the macroscale strain is expected to be equal to zero (see Eq. (1)), it is advantageous to cast this localization relationship in terms of the stress tensor instead of the strain tensor. The localization relationship for the stress field arising from the thermal component is therefore expressed as

$$\boldsymbol{\sigma}_{\mathbf{s}}^{th} = \left(\sum_{h=1}^{H}\sum_{\mathbf{t}\in\mathbf{S}} \boldsymbol{\xi}_{\mathbf{t}}^{h}\, m_{\mathbf{s}+\mathbf{t}}^{h} + \sum_{h=1}^{H}\sum_{h'=1}^{H}\sum_{\mathbf{t}\in\mathbf{S}}\sum_{\mathbf{t}'\in\mathbf{S}} \boldsymbol{\xi}_{\mathbf{t}\mathbf{t}'}^{hh'}\, m_{\mathbf{s}+\mathbf{t}}^{h} m_{\mathbf{s}+\mathbf{t}+\mathbf{t}'}^{h'} + \ldots\right)\theta \tag{8}$$

where $\boldsymbol{\sigma}_{\mathbf{s}}^{th}$ is the local stress tensor in spatial bin $\boldsymbol{s}$ caused by only the thermal component of the imposed strain. $\boldsymbol{\xi}_{\mathbf{t}}^{h}$ and $\boldsymbol{\xi}_{\mathbf{t}\mathbf{t}'}^{hh'}$ are the corresponding first-order and second-order influence coefficients that are now second-rank tensors. This relationship is in complete correspondence with the analytical expression derived from Kroner's theory for a similar problem (Gardner, Adams, Basinger and Fullwood 2009).

Truncating the series in Eq. (8) to the first-order terms, transforming the equation into DFT space, and making use of the constraints expressed in Eq. (6) results in the following expression (derivation is very similar to that of Eq. (7)):

$$\Im_{\mathbf{k}\neq\mathbf{0}}\left(\boldsymbol{\sigma}_{\mathbf{s}}^{th}\right)=\left[\left(\widehat{\boldsymbol{\varphi}}_{\mathbf{k}}^{1}\right)^{*}M_{\mathbf{k}}^{1}\right]\theta,\quad \Im_{\mathbf{0}}\left(\boldsymbol{\sigma}_{\mathbf{s}}^{th}\right)=\mathbf{0},\ \widehat{\boldsymbol{\varphi}}_{\mathbf{k}}^{1}=\left(\boldsymbol{\varphi}_{\mathbf{k}}^{1}-\boldsymbol{\varphi}_{\mathbf{k}}^{2}\right),\ \boldsymbol{\varphi}_{\mathbf{k}}^{h}=\Im_{\mathbf{k}}\left(\boldsymbol{\xi}_{\mathbf{t}}^{h}\right). \tag{9}$$

The expression for $\Im_{\mathbf{0}}\left(\boldsymbol{\sigma}_{\mathbf{s}}^{th}\right)$ in Eq. (9) simply imposes the requirement that the volume average of $\boldsymbol{\sigma}_{\mathbf{s}}^{th}$ over the microscale should be zero. Once the local stress tensor $\boldsymbol{\sigma}_{\mathbf{s}}^{th}$ is computed, it is easy to compute the corresponding local elastic strain tensor (arising from the thermal component alone) and recover the effective thermal expansion coefficients tensor (thermal strain per unit temperature change) in the sample as

$$\widetilde{\boldsymbol{\alpha}}=\frac{1}{|\mathbf{S}|}\sum_{\mathbf{s}\in\mathbf{S}}\left\{\frac{1}{\theta}\mathbf{C}_{\mathbf{s}}^{-1}\boldsymbol{\sigma}_{\mathbf{s}}^{th}+\mathbf{A}_{\mathbf{s}}\right\} \tag{10}$$

where $\mathbf{C}_{\mathbf{s}}$ and $\mathbf{A}_{\mathbf{s}}$ are the local fourth-rank elastic stiffness tensor and the local second-rank thermal expansion coefficient tensor, respectively, in the spatial bin s. These local descriptions may be expressed as volume-averaged values of the microstructure in each bin as:

$$\mathbf{C}_{\mathbf{s}}=\sum_{h=1}^{H}\mathbf{C}^{h}m_{\mathbf{s}}^{h},\quad \mathbf{A}_{\mathbf{s}}=\sum_{h=1}^{H}\mathbf{A}^{h}m_{\mathbf{s}}^{h} \tag{11}$$

where $\mathbf{C}^{h}$ and $\mathbf{A}^{h}$ denote the respective stiffness and thermal expansion tensors of phase h. Since in most experimental datasets, each spatial bin is typically occupied by a single local state, Eq. (11) essentially amounts to assigning the values corresponding to the local states to each spatial bin.

It is reiterated here that influence coefficients $\widehat{\boldsymbol{\beta}}_{\mathbf{k}}^{1}$ and $\widehat{\boldsymbol{\varphi}}_{\mathbf{k}}^{1}$ need to be established only once for a selected material system, because they are expected to be completely independent of the morphology of the microstructure (i.e. $m_{\mathbf{s}}^{h}$). The influence coefficients $\boldsymbol{\alpha}_{\mathbf{t}}^{h}$ are related to Green's functions used in mechanics (Kroner 1977; Kroner 1986). We expect $\boldsymbol{\alpha}_{\mathbf{t}}^{h}\rightarrow\mathbf{0}$ as t takes on large values. Once these coefficients are known, they serve as convolution kernels in estimating the local thermo-elastic field for any arbitrary microstructure (using Eqs. (7) and (9)). For the thermo-elastic response studied here, we will also exploit the superposition principle to account for arbitrary (but uniform) loading conditions at the macroscale. This basic concept was previously validated for purely elastic deformation of two-phase composites

(Landi, Niezgoda et al. 2009), where $\widehat{\boldsymbol{\beta}}_{\mathbf{k}}^{1}$ were established and validated for selected two-phase composite material systems. In this paper, we critically evaluate the extended framework presented here for thermo-elastic deformations in multi-phase composites.

Case Study I: Thermo-Elastic Fields for a Two-Phase Composite

As the first case study, we will examine the thermo-elastic response of a class of two-phase composites (*H=2*) subjected to a uniform temperature change, $\theta = 10\ K$. For simplicity, the two phases will be referred to as "white" and "black". These are both assumed to be isotropic, with Young moduli of $E_1 = 200\ GPa$ and $E_2 = 400\ GPa$, and thermal expansion coefficients of $\alpha_1 = 20 \cdot 10^{-6}\ [K^{-1}]$ and $\alpha_2 = 10 \cdot 10^{-6} [K^{-1}]$ respectively. Poisson's ratio is assumed to be 0.3 for both phases. The properties of the two phases with a contrast ratio of 2 in both Young's moduli ratio and the thermal expansion coefficients would classify this composite as a moderate contrast composite. Based on our earlier work (Landi, Niezgoda et al. 2009), localization relationships with only the first-order influence coefficients are expected to produce reasonably accurate predictions for this class of composites.

The procedures for establishing the influence coefficients $\widehat{\boldsymbol{\beta}}_{\mathbf{k}}^{1}$ were already discussed in our recent work. This was accomplished by calibrating Eq. (7) to results from finite element simulations (Landi, Niezgoda et al. 2009). More specifically, a set of six different periodic uniform boundary conditions were simulated on a set of two "delta" microstructures using finite element models, producing a total of twelve datasets for the calibration process. These delta microstructures consisted of one element of "black" surrounded completely by "white", and vice-versa (see Figure 2). The six different sets of boundary conditions corresponded to three uniaxial strains and three simple shears, respectively. In reality, for the composite with isotropic constituents studied here, the three uniaxial strain datasets are related to each other by simple rotations. The three simple shear datasets are also related to each other in a similar way. The $\widehat{\boldsymbol{\beta}}_{\mathbf{k}}^{1}$ obtained by this procedure were previously validated by comparing the predictions for a set of random microstructures (each spatial location in the RVE randomly assigned to either the black or the white local state) from Eq. (7) to the corresponding predictions for the same microstructures from the finite element simulations (Landi, Niezgoda et al. 2009). Random microstructures were chosen for the validation part of the study because they present a very rich diversity of local neighborhoods in the RVE, and therefore, the most heterogeneous local strain (or stress) fields. The random microstructures represent some of the most difficult validation examples for the proposed localization relationships.

In all the case studies presented in this paper, the FEM results are generated us-

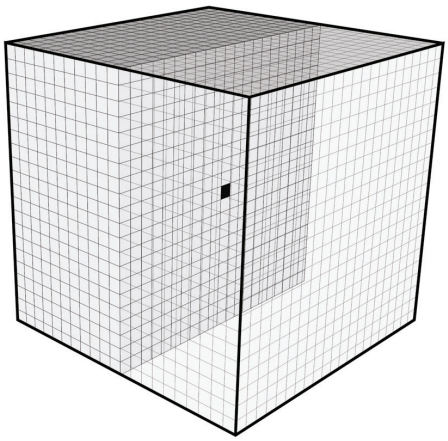

Figure 2: Delta microstructure used to establish the influence coefficients. In this microstructure, a central "black" element is embedded in "white" elements. In a two-phase material system, another delta microstructure can be defined, where a central "white" element is completely surrounded by "black" elements.

ing the commercial software ABAQUS®, where each dataset consists of 9261 (21x21x21) cuboid-shaped three-dimensional eight-noded solid elements (C3D8). The use of cube-shaped elements defines a regularly spaced grid, which is ideal for the computation of DFTs. Additionally, the macroscale strain condition is imposed as a periodic uniform boundary condition on the RVE (Landi, Niezgoda et al. 2009). In our prior experience, we found that the periodic boundary conditions produce numerical datasets that are best suited for DFT representations.

Influence coefficients $\widehat{\boldsymbol{\varphi}}_{\mathbf{k}}^{1}$ were established here using a very similar approach as that described above for $\widehat{\boldsymbol{\beta}}_{\mathbf{k}}^{1}$. The same two eigen microstructures described above (see Figure 2) were used to generate the calibration datasets. These microstructures were subjected to only a prescribed temperature change. Periodic boundary conditions are imposed on the dataset by relating displacements of nodes on opposite faces to each other (Landi, Niezgoda et al. 2009). The results from these two finite element simulations were used to calibrate Eq. (9) and estimate $\widehat{\boldsymbol{\varphi}}_{\mathbf{k}}^{1}$. For validation of these influence coefficients, we consider once again random microstructures. Figure 3 shows an example random microstructure used here for validation. The internal stress fields in this RVE when subjected to a purely thermal loading of 10 K were predicted using Eq. (9). This approach will hereafter be referred to as the Spectral Method. The corresponding strain field in the RVE was recovered using

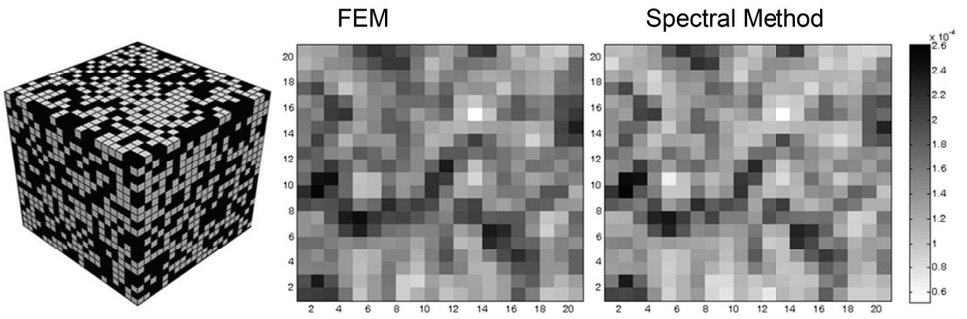

Figure 3: Comparison of contour maps of the local $\boldsymbol{\varepsilon}_{11}$ component of strain for the mid-plane of a 3-D digitally created random microstructure (left), calculated using the FEM analysis (center) and the proposed DFT-based localization relationships referred as the Spectral Method (right). The 3-D dataset is subjected to a temperature increase of temperature of 10 K without any additional mechanical loading. The ratio of the Young's moduli and the thermal expansion coefficients for the two phases were both assumed to be 2 in this case study.

elastic stress-strain relationships for the material present in each spatial bin. The predictions of the internal strain fields in the RVE from both the FE and the Spectral methods are compared against each other in Figure 3.

In order to better quantify the accuracy of the predictions from the Spectral Method, we define an error measure for each spatial bin of the RVE as

$$Err_{\mathbf{s}} = \frac{((\boldsymbol{\varepsilon}_{\mathbf{s}})_{11})_{FEM} - ((\boldsymbol{\varepsilon}_{\mathbf{s}})_{11})_{SM}}{\overline{\boldsymbol{\varepsilon}}_{11}} \cdot 100 \tag{12}$$

where the subscripts FEM and SM indicate that the predictions were made using FEM and Spectral Methods, respectively, while $\overline{\boldsymbol{\varepsilon}}_{11}$ corresponds to the volume averaged strain experienced by the dataset. Based on the above definition, the maximum value of $Err_{\mathbf{s}}$ across the 3D dataset is only 0.1%. Also, the DFT-based predictions for the random microstructure in Figure 3 took only 0.6 seconds on a typical desktop computer (2.00 GHz CPU and 4GB RAM), while the FEM method on the same machine took 113 seconds.

The effective thermal expansion coefficients tensor for the random microstructure shown in Figure 3 was computed using Eq. (10), and compared to the corresponding predictions from the FE model in Table 1. It is seen that the predictions for all components of the thermal expansion coefficients tensor from the Spectral Method are in excellent agreement with those from the FE Model. It should also be noted

that these predictions do not invoke any simplifying assumptions based on symmetry at the macroscale.

Let us now consider a thermo-mechanical loading condition on the same RVE. Let us assume that the total strain imposed on the RVE is a uniaxial strain tensor with $\overline{\boldsymbol{\varepsilon}}_{11} = 0.0005$ (all of the other components of the macroscale strain tensor being

Table 1: Comparison of the components of the effective thermal expansion coefficient tensor $\widetilde{\boldsymbol{\alpha}}$ predicted by the FEM and the Spectral Method for the random microstructure shown in Figure 3.

Spectral Method	FEM
$\tilde{\alpha}_{11} = 14.067 \cdot 10^{-6}\ [K^{-1}]$	$\tilde{\alpha}_{11} = 14.03 \cdot 10^{-6} [K^{-1}]$
$\tilde{\alpha}_{22} = 14.046 \cdot 10^{-6} [K^{-1}]$	$\tilde{\alpha}_{22} = 14.015 \cdot 10^{-6} [K^{-1}]$
$\tilde{\alpha}_{33} = 14.074 \cdot 10^{-6} [K^{-1}]$	$\tilde{\alpha}_{33} = 14.045 \cdot 10^{-6} [K^{-1}]$
$\tilde{\alpha}_{12} = 14.993 \cdot 10^{-9} [K^{-1}]$	$\tilde{\alpha}_{12} = 14.911 \cdot 10^{-9} [K^{-1}]$
$\tilde{\alpha}_{13} = 14.998 \cdot 10^{-9} [K^{-1}]$	$\tilde{\alpha}_{13} = 14.952 \cdot 10^{-9} [K^{-1}]$
$\tilde{\alpha}_{23} = 14.992 \cdot 10^{-9} [K^{-1}]$	$\tilde{\alpha}_{23} = 14.936 \cdot 10^{-9} [K^{-1}]$

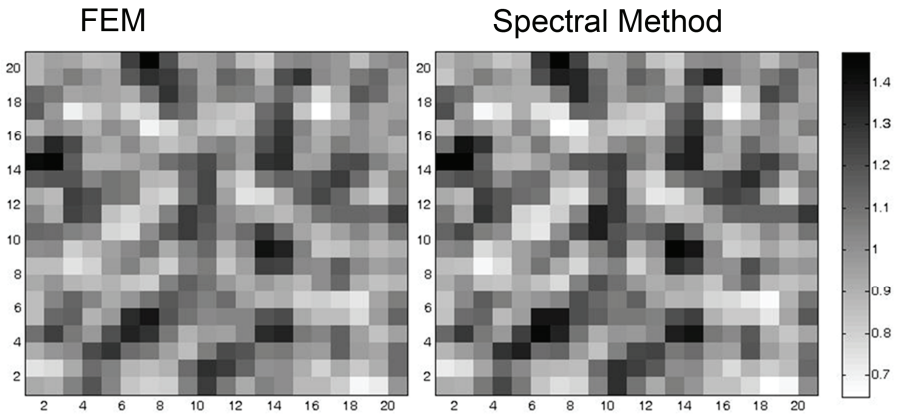

Figure 4: Comparison of contour maps of the local $\boldsymbol{\varepsilon}_{11}$ component of strain normalized by the average strain applied (0.0005) for the mid-plane of the 3D digitally created random microstructure presented in Figure 3, calculated using the FEM analysis (left) and the Spectral Method (right). The RVE is subjected simultaneously to a temperature change of 10 K and a total uniaxial strain tensor with $\overline{\boldsymbol{\varepsilon}}_{11} = 0.0005$. The ratios of the Young's moduli and the thermal expansion coefficients for the two phases were assumed to be 2 for this case study.

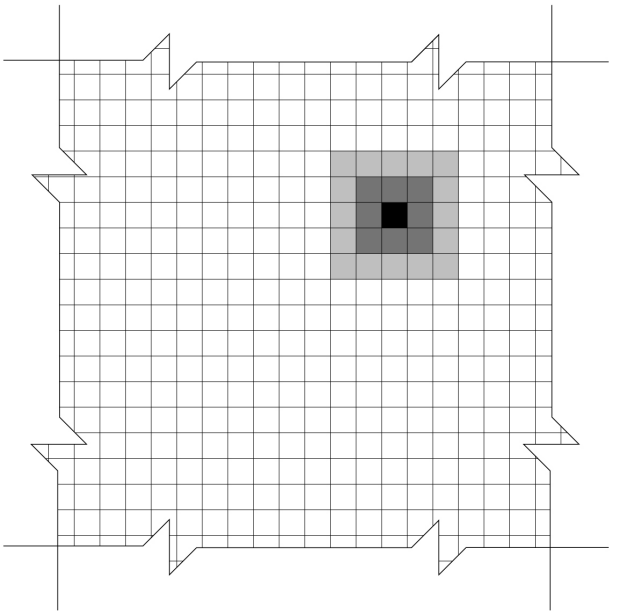

Figure 5: Schematic representation of the grouping of the contributions to the local strain in each spatial bin. In Table 2, the contributions are separated into three groups: (i) self-contribution from the cell itself (shaded in black), (ii) contribution from the first layer of neighbors (shaded in dark grey), and (iii) contribution from the second layer of neighbors (shaded in lighter grey).

equal to zero) along with the simultaneous temperature increase of $\theta = 10K$. For this loading, we have to decompose the total strain into two components as described earlier: (i) a mechanical component, and a (ii) thermal component. The thermal component is essentially given by $\widetilde{\boldsymbol{\alpha}}\theta$, with $\widetilde{\boldsymbol{\alpha}}$ already computed in Table 1. This allows us to compute the mechanical component as $\overline{\boldsymbol{\varepsilon}}^m = \left(\overline{\boldsymbol{\varepsilon}} - \widetilde{\boldsymbol{\alpha}}\theta\right)$, and to compute the corresponding local strain field using Eq. (7). The local total strain field in the RVE is then computed by adding the mechanical component to the thermal component shown in Figure 3. Figure 4 compares the prediction for the local total strain field for this thermo-mechanical loading condition from the Spectral Method with the corresponding prediction from the FE analysis. The maximum value of $Err_{\mathbf{s}}$, as defined by Eq. (12), across the entire 3-D dataset was still only about 0.1%, consistent with the error noted in the earlier example with only the thermal loading.

An important feature of the localization relationships presented here is the ability to

separately compute the individual contributions from all neighbors of a spatial bin in the RVE. The neighbors for a spatial bin of interest can be conveniently grouped by the number of layers that separate them from the spatial bin of interest. This grouping is shown schematically for a 2-D microstructure in Figure 5. Although the concept is described for the 2-D case in Figure 5, it is trivially extended and applied to 3-D microstructures in this study.

Intuitively, we expect the influence of a given spatial bin to decrease as we move away from the bin. We also expect the influence zone to be larger for higher contrast composite systems. For the RVE shown in Figure 3, the contributions to the $\boldsymbol{\varepsilon}_{11}$ component of the local strain in each spatial bin predicted by the Spectral Method were analyzed, and the overall statistics are reported in Table 2. The contributions are grouped into three parts depending on where they come from: (i) the spatial bin of interest itself referred to as the "self contribution", (ii) the first layer of neighboring bins (a total of 26 bins), and (iii) the second layer of neighboring bins (a total of 98 bins). The results are shown for two different values of contrast in the properties of the constituents and two loading cases (a purely mechanical load and a purely thermal load, respectively) on the random microstructure shown in Figure 3. The results shown in Table 2 clearly indicate that the influence zone around a spatial bin of interest is largely confined to the first layer around it for the low contrast composites. On the other hand, the influence zone is larger for composites with a higher contrast. These observations indicate that it should be possible to get reasonably accurate predictions for the local fields in low contrast composites by just accounting for the first layer of neighbors. It is important to recognize that the results presented in Table 2 are specifically for the microstructure shown in Figure 3. These results are expected to be strongly influenced by the details of the microstructure.

The influence coefficients implicitly capture the underlying physics of spatial interactions in the system for the prescribed boundary conditions. In the spectral approach, the local response is strongly correlated to the spatial distribution of the local states in the neighborhood of the spatial location of interest. These relationships are cast in simple algebraic forms in Eqs. (3) and (8), and can be potentially inverted to identify specific microstructures that meet certain selected design specifications. Although, rigorous inverse methods of microstructure design are beyond the scope of the present work, we explore here a simple example to illustrate the advantages of the Spectral Method described in this paper in identifying optimal microstructures.

Let us consider the two-phase material system already introduced (contrast ratio of 2 for both the Youngs' moduli and the thermal expansion coefficients of the two phases), subjected to a purely thermal load (applied temperature change $\theta =$

Table 2: Average contributions from different layers of neighboring spatial bins to the local $\boldsymbol{\varepsilon}_{11}$component of strain for the RVE shown in Figure 3 in two loading conditions: (i) a purely mechanical loading, and (ii) a purely thermal loading. The results are shown for two different levels of contrasts in the local properties of the constituents. SD in the table refers to standard deviation.

	Pure Thermal Load $\theta = 10\ K$			Pure Mechanical Load $\overline{\boldsymbol{\varepsilon}}_{11} = 0.0005$		
	Self-Contribution	1st Layer Contribution	2nd Layer Contribution	Self-Contribution	1st Layer Contribution	2nd Layer Contribution
$\frac{E_1}{E_2} = 2 \quad \frac{\alpha_1}{\alpha_2} = 2$	83.3% SD = 2.4	12.3% SD = 2.9	3.8% SD = 1.7	90.7% SD = 3.0	6.2% SD = 1.9	2.9% SD = 1.1
$\frac{E_1}{E_2} = 2 \quad \frac{\alpha_1}{\alpha_2} = 5$	62.5% SD = 2.8	19.3% SD = 3.9	12.7% SD = 2.1			
$\frac{E_1}{E_2} = 5 \quad \frac{\alpha_1}{\alpha_2} = 2$	72.9% SD = 5.0	20.3% SD = 5.8	5.2% SD = 2.7	74.9% SD = 5.9	17.3% SD = 3.1	4.2% SD = 1.7
$\frac{E_1}{E_2} = 5 \quad \frac{\alpha_1}{\alpha_2} = 5$	45.8% SD = 4.5	34.0% SD = 6.2	14.1% SD = 2.9			

10 K). As noted earlier, the influence coefficients reflect the contribution arising from placement of a particular local state ("black" or "white") in any spatial bin of the microstructure on the response variable of interest (e.g. stress or strain) in any other spatial bin in the microstructure. Accounting for the redundancies of Eq. (6) in Eq. (8) (this is equivalent to performing an inverse DFT of Eq. (9)) allows us to express the implicit first-order structure-response correlation for low contrast composites as:

$$\boldsymbol{\sigma}_{\mathbf{s}}^{th} = \left(\sum_{\mathbf{t} \in \mathbf{S}} \left(\boldsymbol{\xi}_{\mathbf{t}}^{1} - \boldsymbol{\xi}_{\mathbf{t}}^{2} \right) m_{\mathbf{s}+\mathbf{t}}^{1} + \sum_{\mathbf{t} \in \mathbf{S}} \boldsymbol{\xi}_{\mathbf{t}}^{2} \right) \theta \tag{13}$$

In the examples explored in this paper, the microstructures are defined such that each spatial bin is allowed to contain only one of the local states (i.e. eigen microstructures (Adams, Gao et al. 2005)). For such microstructures, the microstructure function $m_{\mathbf{s}}^{h}$ is allowed to take only one of the two values: 0 or 1 (see Figure 1).

Therefore, there is a contribution to the local stress only when $m^1_{\mathbf{s+t}} = 1$. Furthermore, a positive value of the influence coefficient $\left(\boldsymbol{\xi}^1_{\mathbf{t}} - \boldsymbol{\xi}^2_{\mathbf{t}}\right)$ would indicate that the contribution increases the local stress in spatial bin s when the local state 1 is placed in bin s+t. Likewise, this contribution decreases the local stress if the influence coefficient $\left(\boldsymbol{\xi}^1_{\mathbf{t}} - \boldsymbol{\xi}^2_{\mathbf{t}}\right)$ is negative valued. As a result, the maximum tensile local stress is achieved by arranging the local states in such a way that the spatial locations corresponding to positive values of $\left(\boldsymbol{\xi}^1_{\mathbf{t}} - \boldsymbol{\xi}^2_{\mathbf{t}}\right)$ are filled with local state 1 (other spatial bins are automatically filled with the other local state). Figure 6 shows the values of the influence coefficients $\left(\boldsymbol{\xi}^1_{\mathbf{t}} - \boldsymbol{\xi}^2_{\mathbf{t}}\right)$ for the spatial bins in the first layer of neighbors for the $\boldsymbol{\sigma}_{11}$ stress component in a purely thermal loading condition.

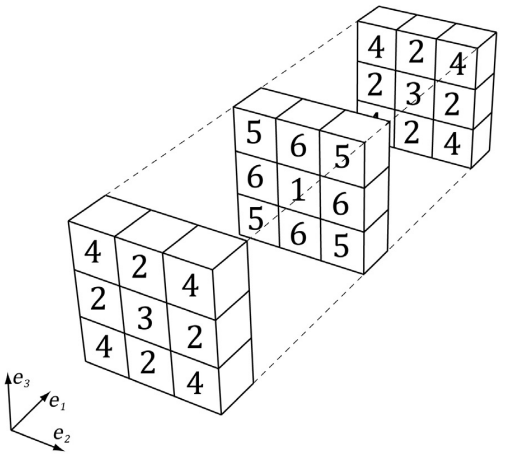

Group	$(\xi^1_t - \xi^2_t)$ $[MPa \cdot K^{-1}]$
1	*3.7350*
2	*0.1751*
3	*0.1150*
4	*0.0886*
5	*-0.129*
6	*-0.671*

Figure 6: The values of the $\left(\boldsymbol{\xi}^1_{\mathbf{t}} - \boldsymbol{\xi}^2_{\mathbf{t}}\right)$ influence coefficients for the spatial bins in the first layer of neighbors for the $\boldsymbol{\sigma}_{11}$ stress component in a purely thermal loading condition. This set of coefficients applies to a 2-phase isotropic material where the ratio of Youngs' moduli and the thermal expansion coefficients for the two phases are both 2. The influence coefficients for the 27 first-neighbors are grouped into 6 different sets, numbered in decreasing order of magnitude. These account for the major part of the total $\boldsymbol{\sigma}_{11}$ stress experienced by the central cell (see Table 2).

Six different values of the influence coefficients can be identified among the first neighbors for the present problem, as depicted in Figure 6. For the two-phase composite selected here, local state 1 corresponded to the black phase with the higher modulus and the lower thermal expansion coefficient. The first-neighbor influence

coefficients in Figure 6 indicate that a black element completely surrounded by white first-neighbors will result in a tensile stress of 3.735 $[MPa \cdot K^{-1}]$ (for one degree increase in temperature). This is because only the spatial bins occupied by the black phase make a contribution to the computations in Eq. (13). Conversely, a white element completely surrounded by black elements results in a compressive stress of 0.8604 $[MPa \cdot K^{-1}]$ (here all elements except the central one contribute to the computations in Eq. (13)). Figure 6 indicates that the highest tensile stress of 6.0746 $[MPa \cdot K^{-1}]$ occurs when a black phase is placed in locations identified by 1, 2, 3, and 4 in Figure 6 (all other locations being occupied by the white phase). For the same configuration, inverting the locations of white and black phases results in the highest compressive stress of 3.2 $[MPa \cdot K^{-1}]$ in the central cell.

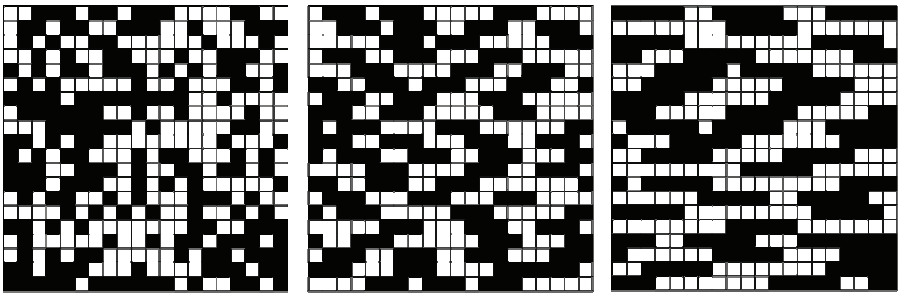

Figure 7: Three different microstructures have been selected to study the effect of morphology change on the stress field, for selected loading condition. The first microstructure is the random microstructure already introduced in Figure 3 (left) with cube-shaped inclusions; the second one (center) has rods of dimensions 3x1x1 oriented along the e_1 direction; and the third one (left) has longer rods of dimensions 5x1x1, also oriented along the e_1 direction. The volume fraction of both black and white phases in each microstructure was kept constant at about 50%.

The influence coefficients therefore provide tremendous insights into how specific topologies contribute to the microscale response fields of interest. Next, we examine critically the error introduced by ignoring the contributions from spatial bins beyond the first layer of neighbors. For this purpose, we plotted the stress distributions in both constituent phases computed in three different ways for selected microstructures: (i) Finite element analyses, (ii) Spectral Method using all the contributions from all spatial bins, and (iii) Spectral Method using only the self-contribution and the contribution from the first layer of neighbors. Three different microstructures, whose mid-sections are shown in Figure 7, were selected for this comparison. The volume fraction of both black and white phases in each microstructure was kept

about 50%, but their morphologies were altered substantially: the first microstructure being the random microstructure presented in Figure 3; the second one is made of short rods oriented along the e_1 direction; and the third is one made of longer rods (or fibers), also oriented along the e_1 direction.

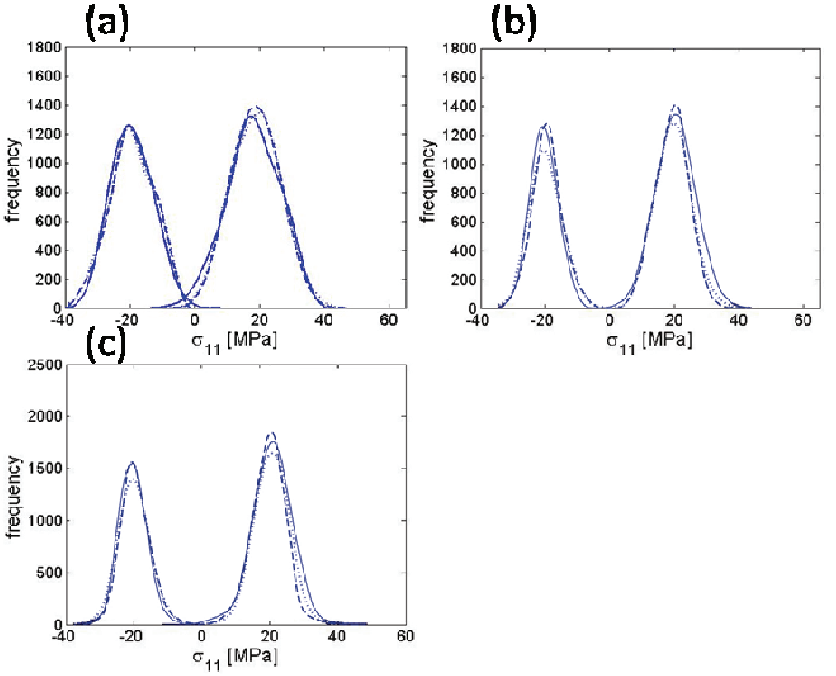

Figure 8: $\boldsymbol{\sigma}_{11}$ stress distributions in both constituent phases for the three microstructures shown in Figure 7: (a) Cube shaped inclusions, (b) Short rod shaped inclusions, and (c) Long rod shaped inclusions. The results are obtained using three different methods: (i) FEM analyses (solid line), (ii) Spectral Method using all the contributions from all spatial bins (dashed line), and (iii) Spectral Method using only the self-contribution and the contribution from the first layer of neighbors (dotted line).

It is seen from Figure 8 that the $\boldsymbol{\sigma}_{11}$ stress distributions in each phase get sharper and move farther apart as the shape of the reinforcement phase is changed from a cube to a short rod to a long rod. It is also seen that there is excellent agreement between the predictions of the Spectral Method (with all neighbors included) and the finite element results. Furthermore, there appears to be only a small error in ignoring the contributions from spatial bins beyond the first layer of neighbors for this low contrast composite.

Case study II: Extension to Multi-Phase Composites

In the previous case study, we have demonstrated the accuracy of the localization relationships in Eq. (7) and Eq. (9) for two-phase composites. We now consider an example where these relationships are applied to a three-phase composite (which can then be easily extended to a multi-phase composite). For a three-phase composite, *H=3*. Eqs. (7) and (9) re-derived for this case take the following form:

$$\begin{aligned} &\Im_{\mathbf{k}\neq\mathbf{0}}\left(\boldsymbol{\varepsilon}_{\mathbf{s}}^{m}\right)=\left[\left(\widehat{\boldsymbol{\beta}}_{\mathbf{k}}^{1}\right)^{*}M_{\mathbf{k}}^{1}+\left(\widehat{\boldsymbol{\beta}}_{\mathbf{k}}^{2}\right)^{*}M_{\mathbf{k}}^{2}\right]\left(\overline{\boldsymbol{\varepsilon}}^{m}\right),\ \ \Im_{\mathbf{0}}\left(\boldsymbol{\varepsilon}_{\mathbf{s}}^{m}\right)=|\mathbf{S}|\,\overline{\boldsymbol{\varepsilon}}^{m},\\ &\widehat{\boldsymbol{\beta}}_{\mathbf{k}}^{1}=\left(\boldsymbol{\beta}_{\mathbf{k}}^{1}-\boldsymbol{\beta}_{\mathbf{k}}^{3}\right),\ \ \widehat{\boldsymbol{\beta}}_{\mathbf{k}}^{2}=\left(\boldsymbol{\beta}_{\mathbf{k}}^{2}-\boldsymbol{\beta}_{\mathbf{k}}^{3}\right). \end{aligned} \tag{14}$$

$$\begin{aligned} &\Im_{\mathbf{k}\neq\mathbf{0}}\left(\boldsymbol{\sigma}_{\mathbf{s}}^{th}\right)=\left[\left(\widehat{\boldsymbol{\varphi}}_{\mathbf{k}}^{1}\right)^{*}M_{\mathbf{k}}^{1}+\left(\widehat{\boldsymbol{\varphi}}_{\mathbf{k}}^{2}\right)^{*}M_{\mathbf{k}}^{2}\right]\theta,\ \ \Im_{\mathbf{0}}\left(\boldsymbol{\sigma}_{\mathbf{s}}^{th}\right)=\mathbf{0},\\ &\widehat{\boldsymbol{\varphi}}_{\mathbf{k}}^{1}=\left(\boldsymbol{\varphi}_{\mathbf{k}}^{1}-\boldsymbol{\varphi}_{\mathbf{k}}^{3}\right),\ \ \widehat{\boldsymbol{\varphi}}_{\mathbf{k}}^{2}=\left(\boldsymbol{\varphi}_{\mathbf{k}}^{2}-\boldsymbol{\varphi}_{\mathbf{k}}^{3}\right). \end{aligned} \tag{15}$$

Following the methodology described earlier for establishing the values of the influence coefficients, we seek to calibrate Eqs. (14) and (15) to corresponding results from FE analyses on delta microstructures (see Figure 2). For the three-phase composite, we have six potential delta microstructures. However, the form of Eqs. (14) and (15) suggests that the influence coefficients can be established by considering two phases at a time. In other words, it should be possible to consider two-phase composites comprising phases 1 and 3 to evaluate $\widehat{\boldsymbol{\beta}}_{\mathbf{k}}^{1}$ and $\widehat{\boldsymbol{\varphi}}_{\mathbf{k}}^{1}$ likewise, and then subsequently consider two-phase composites comprising phases 2 and 3 to evaluate $\widehat{\boldsymbol{\beta}}_{\mathbf{k}}^{2}$ and $\widehat{\boldsymbol{\varphi}}_{\mathbf{k}}^{2}$. If this uncoupling provides reasonably accurate estimates of the influence coefficients, it will dramatically reduce the computational effort involved in establishing the influence coefficients for multi-phase composites.

In order to validate the above approach, we consider a composite comprising three isotropic phases with Young moduli of 200, 300 and 400 GPa, respectively. The Poisson's ratio is assumed to be 0.3 for all phases. The thermal expansion coefficients are assumed to be $20\cdot10^{-6}$, $15\cdot10^{-6}$ and $10\cdot10^{-6}$ $[K^{-1}]$ respectively. For this three-phase composite, we have established the influence coefficients $\widehat{\boldsymbol{\beta}}_{\mathbf{k}}^{1}$, $\widehat{\boldsymbol{\beta}}_{\mathbf{k}}^{2}$, $\widehat{\boldsymbol{\varphi}}_{\mathbf{k}}^{1}$, and $\widehat{\boldsymbol{\varphi}}_{\mathbf{k}}^{2}$ using only four of the six delta microstructures that allow us to decouple these sets of coefficients in the calibration process as described above.

The predictions from influence coefficients established using this method were compared against corresponding predictions from FE analyses for a thermo-mechanical loading condition involving a macroscale uniaxial total strain tensor with $\overline{\boldsymbol{\varepsilon}}_{11}=0.0005$ and a simultaneous temperature increase of 10 K. These results are summarized in Figure 9.

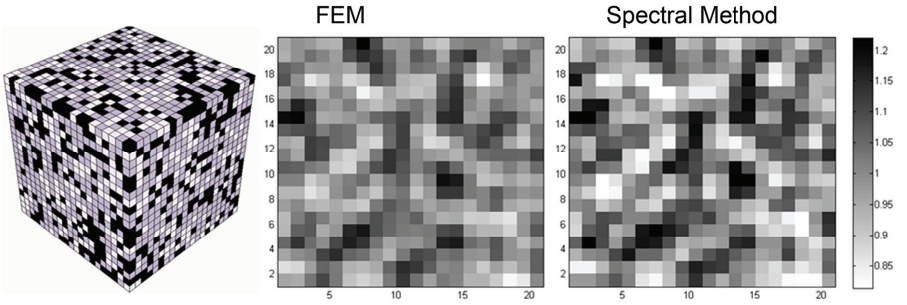

Figure 9: Comparison of contour maps of the local $\boldsymbol{\varepsilon}_{11}$ component of strain (normalized by the average strain applied) for the mid-plane of a 3D three-phase random microstructure (left), calculated using the FEM analysis (center) and the Spectral Method (right). The three phases were assumed to be isotropic, with Young moduli of 200, 300 and 400 GPa, respectively, while Poisson ratio is assumed to be 0.3 for all phases. The thermal expansion coefficients are assumed to be $20 \cdot 10^{-6}$, $15 \cdot 10^{-6}$ and $10 \cdot 10^{-6}$ $[K^{-1}]$ respectively. The dataset is subjected simultaneously to a temperature change of 10 K and an uniaxial macroscopic strain $\overline{\boldsymbol{\varepsilon}}_{11} = 0.0005$.

Based on the definition of error in Eq. (12), the average value of Err in the results shown in Figure 9 was about 2.4%. Furthermore, only 0.7 seconds of CPU time was necessary for the Spectral Method on a standard desktop computer, while the FEM analysis on the same machine required 119 seconds.

3 Conclusions

A novel framework has been presented for predicting the response fields in multi-phase composites subjected to thermo-mechanical loading conditions. In this novel approach, the localization relationships take on a simple structure expressed as a series sum, where each term in the series is a convolution product of local structure and the governing physics expressed in the form of influence coefficients. In particular, it was noted that the self-contribution and the contribution from the first layer of neighbors accounted for the major component of the local response for low contrast composites. The influence coefficients were shown to provide important insights into the influence of microstructure topology on the microscale response field.

Acknowledgement: The authors acknowledge financial support for this work

from the DARPA-ONR Dynamic 3D Digital Structure project, Award No. N000140-510504 (Program Manager: Dr. Julie Christodoulou).

References

Adams, B. L., X. Gao, S. R. Kalidindi (2005): Finite approximations to the second-order properties closure in single phase polycrystals. *Acta Materialia* 53(13): 3563-3577.

Adams, B. L., T. Olson (1998): The mesostructure - properties linkage in polycrystals. *Progress in Materials Science* 43(1): 1-87.

Beran, M. J. (1968): *Statistical continuum theories*. New York, Interscience Publishers.

Binci, M., D. Fullwood, S. R. Kalidindi (2008): A new spectral framework for establishing localization relationships for elastic behavior of composites and their calibration to finite-element models. *Acta Materialia* 56(10): 2272-2282.

Briggs, W. L., V. E. Henson (1995): *The DFT : an owner's manual for the discrete Fourier transform*. Philadelphia, Society for Industrial and Applied Mathematics.

Duvvuru, H. K., X. Wu, S. R. Kalidindi (2007): Calibration of elastic localization tensors to finite element models: Application to cubic polycrystals. *Computational Materials Science* 41(2): 138-144.

Fullwood, D. T., S. R. Kalidindi, B. L. Adams, S. Ahmadi (2009): A Discrete Fourier Transform Framework for Localization Relations. *CMC: Computers Materials & Continua* 9(1): 25-39.

Fullwood, D. T., S. R. Niezgoda, B. L. Adams, S. R. Kalidindi (2009): Microstructure Sensitive Design for Performance Optimization. *Journal of Progress in Materials Science* in press.

Fullwood, D. T., S. R. Niezgoda, S. R. Kalidindi (2008): Microstructure reconstructions from 2-point statistics using phase-recovery algorithms. *Acta Materialia* 56(5): 942-948.

Gardner, A. J., B. L. Adams, J. Basinger, D. T. Fullwood (2009): ESBD-based continuum dislocation microscopy. *International Journal of Plasticity* in press.

Garmestani, H., S. Lin, B. L. Adams (1998): Statistical Continuum Theory for Inelastic Behavior of a Two-phase Medium. *International Journal of Plasticity* 14(8): 719-731.

Garmestani, H., S. Lin, B. L. Adams, S. Ahzi (2001): Statistical Continuum Theory for Large Plastic Deformation of Polycrystalline Materials. *Journal of the Mechanics and Physics of Solids* 49(3): 589-607.

Hill, R. (1952): The elastic behavior of a crystalline aggregate. Proceedings of the Royal Society of London. Series A, *Mathematical and Physical Sciences* 65: 349-54.

Kalidindi, S. R., M. Binci, D. Fullwood, B. L. Adams (2006): Elastic properties closures using second-order homogenization theories: Case studies in composites of two isotropic constituents. *Acta Materialia* 54(11): 3117-3126.

Kalidindi, S. R., G. Landi, D. T. Fullwood (2008): Spectral representation of higher-order localization relationships for elastic behavior of polycrystalline cubic materials. *Acta Materialia* 56(15): 3843-3853.

Kalidindi, S. R., S. R. Niezgoda, G. Landi, S. Vachhani, A. Fast (2010): A novel framework for building materials knowledge systems. *CMC: Computers Materials & Continua* 395, pp.1-23.

Kroner, E. (1977): Bounds for effective elastic moduli of disordered materials. *Journal of the Mechanics and Physics of Solids* 25(2): 137-155.

Kroner, E. (1986): Statistical modelling, in: J. Gittus, J. Zarka (Eds.), *Modeling small deformation in polycrystals*, Elsevier Science Publishers.

Landi, G., S. R. Niezgoda, S. R. Kalidindi (2009): Multi-scale modeling of elastic response of three-dimensional voxel-based microstructure datasets using novel DFT-based knowledge systems. *Acta Materialia* Submitted.

Lin, S., H. Garmestani (2000): Statistical continuum mechanics analysis of an elastic two-isotropic-phase composite material. *Composites Part B: Engineering* 31(1): 39-46.

Mason, T. A., B. L. Adams (1999): Use of microstructural statistics in predicting polycrystalline material properties. *Metallurgical and Materials Transactions A: Physical Metallurgy and Materials Science* 30(4): 969-979.

Niezgoda, S. R., D. T. Fullwood, S. R. Kalidindi (2008): Delineation of the space of 2-point correlations in a composite material system. *Acta Materialia* 56(18): 5285-5292.

Saheli, G., H. Garmestani, B. L. Adams (2004): Microstructure design of a two phase composite using two-point correlation functions. *Journal of Computer-Aided Materials Design* 11 (2-3): 103-115.